

Research Article

# Stability Evaluation of Massive Landslides Using Ensembled Analysis of Time-Series InSAR and Numerical Simulation along the Yellow River, Northwestern of China

Chengcheng Tian,<sup>1,2</sup> Hao Tian ,<sup>1,2</sup> Chunyang Li,<sup>1,2</sup> and Feifei Chen<sup>1,2</sup>

<sup>1</sup>*Qinghai Survey Institute of Hydrogeology and Engineering & Environmental Geology, Xining, 810000 Qinghai, China*

<sup>2</sup>*Qinghai Provincial Key Laboratory of Hydrogeology and Geothermal Geology, Xining, 810000 Qinghai, China*

Correspondence should be addressed to Hao Tian; tianhao13897660096@163.com

Received 16 March 2022; Accepted 26 April 2022; Published 21 May 2022

Academic Editor: Long Yan

Copyright © 2022 Chengcheng Tian et al. This is an open access article distributed under the Creative Commons Attribution License, which permits unrestricted use, distribution, and reproduction in any medium, provided the original work is properly cited.

Loess landslides are a major geological disaster in the southeastern Qinghai Province, causing huge economic losses and casualties. The particularity of loess determines the disaster initiation mechanism, disaster mode, genetic mechanism, and complexity of the evolution process. This paper studies the deformation and stability analysis of the Quwajiasa large-scale multislip loess landslide in the Yellow River Basin from the perspective of field investigation, Interferometric Synthetic Aperture Radar (InSAR) monitoring, and numerical simulation. This study determines the deformation characteristics and genetic mechanism of the landslide through on-site field investigation, then quantitatively evaluates the overall deformation of the landslide using InSAR monitoring, locates the strong deformation area, and finally determines the control relationship between the two sliding surfaces on the landslide deformation using FLAC3D numerical simulation, obtaining the stability coefficient of the two sliding surfaces. The landslide is divided into seven engineering geological zones. The deformation history of the landslide is studied using InSAR technology. Results show that the landslide can be divided into significant deformation areas and no significant deformation areas. Two strong deformation areas are found. The FLAC3D numerical simulation results show that the deformation and stability of the right side of landslide are controlled by sliding surface 1, and the deformation and stability of the left side are controlled by sliding surface 2. The landslide is in an unstable state overall. The research done in this paper proposes a basis for the treatment of the Quwajiasa landslide.

## 1. Introduction

During the Quaternary, ossification created large amounts of aeolian sediments, which form yellowish, carbonate-bearing, quartz-rich, silt-dominated strata called loess [1]. Loess is widely distributed in Asia, Europe, North America, and South America [2]. In China, loess is concentrated in the Loess Plateau. The loess area is 630,000 square kilometers and accounts for 6.63% of the land area. Due to its high porosity, strong water sensitivity, and joint and fracture development, loess collapse, landslides, and ground fissures are common in loess areas [3]. The stability of slopes and natural slopes has always attracted the attention of scholars [4]. According to statistics, 1/3 of all landslides occur in

the loess area. Loess landslides are commonly accompanied by a series of major disasters in the affected areas, including traffic interruption, river blockage, destruction of farmland, factories and mines, and even burial of livestock, people, and villages [5]. Rainfall commonly induces landslide instability, and loess landslides are no exception [6], but the specific properties of loess determine the disaster mechanism, disaster formation mode, genetic mechanisms, and evolution process of loess disasters, which are significantly different from those in other regions and other rock and soil mass. Technologies and methods used on other soil and rock masses do not apply to loess deposits.

Landslide surface deformation is the most intuitive indicator of landslide stability and has been a hot research topic

[7–11]. Geological hazards have always been the focuses of scholars, which have been studied with different methods [12, 13]. Interferometric Synthetic Aperture Radar (InSAR) can provide a large-range of microdeformation information as well as long-term sequence of slow surface deformation and is widely used in landslide research [9, 14, 15]. In recent years, numerous scholars have carried out a series of studies on loess landslides using InSAR technology. Liu et al. studied the deformation history and failure mechanisms of small-scale loess landslides in the Heifangtai loess terrace in Gansu Province using multisource synthetic aperture radar (SAR) data [16], which provides a good precursor for the detection of small-scale loess landslides. Cao et al. used field investigation, optical remote sensing interpretation, and Interferometric Synthetic Aperture Radar (InSAR) to estimate the source material quality in xulonggou (xlg) debris flow in China [17], demonstrating the superiority of the multisource method formed by the combination of InSAR and other methods to solve practical problems. Bayer et al. used InSAR to record the deformation history of four dormant deep landslides reactivated by the excavation of a double track tunnel in the northern Apennine mountains of Italy [18]. Takada et al. studied the spatiotemporal behavior of a large-scale landslide in Onnebetsu-dake mountain, Japan, using InSAR technology [19].

With the development of information technology, numerical analysis has become an important means of analyzing slopes. Since Bowson and Rothf et al. used the strength reduction method to compile FLAC to calculate the safety factor of a slope, a large number of documents and results from numerical simulation analysis of slopes have emerged, which have been widely applied to loess landslides. Wang et al. used the finite element software platform FLAC3D for secondary development and proposed a strength reduction method considering rheological properties [20]. Mu et al. used FLAC3D software to simulate the formation mechanism of a surface landslide under different slope angles within the Shendong mining area and provided a scientific basis for the effective prevention and control of geological disasters through the stability analysis of a goaf collapse slope in a loess gully region [21]. Wang et al. used FLAC3D to analyze the influence of groundwater on FoS of a dump slope and found the engineering solution [22]. He et al. used FLAC three-dimensional numerical simulation to evaluate the treatment effect of compaction pile composite foundation and further demonstrated the feasibility of compaction pile composite foundation in a collapsible loess area [23]. Wang et al. used FLAC3D to build an anchoring model for a loess vertical slope and found that the modified pile unit was suitable for simulating the loess slope reinforced by anchor [24]. The application of FLAC3D numerical simulation is well developed, and the stability analysis of loess landslide has always been an important step in the process of landslide. Therefore, the stability analysis of loess landslide using FLAC3D is a very good method for analyzing loess landslides.

Therefore, in this study, we studied the deformation and stability of loess landslides with multiple sliding surfaces in the Yellow River Basin using field investigation, InSAR mon-

itoring, and numerical simulation. Firstly, a qualitative evaluation of the Quwajiasi landslide is carried out by field investigation, and engineering geological zoning is carried out. Then, the deformation history of the landslide is studied using the small baseline subset (SBAS) time series method. The strong deformation area and the weak deformation area are identified, and the abnormal deformation area is found. The results are compared with field survey results for verification. Finally, the stability coefficient of the landslide is obtained using FLAC3D numerical simulation, which provides the basis for the treatment of the Quwajiasi landslide. This paper is aimed at solving the problem of deformation analysis and stability evaluation of multisliding loess landslides in the Yellow River Basin using InSAR, numerical simulation, and traditional field investigation. The method and results presented in this study provide a good case for the study of complex large loess landslides.

## 2. Geological Setting

As shown in Figure 1, the study area is located in Lajia Town, Maqin County, Qinghai Province (the coordinates are  $100^{\circ}37'55''$ - $100^{\circ}38'59''$ E,  $34^{\circ}40'07''$ - $34^{\circ}40'52''$ N). The study area is located on the South Bank of the Yellow River, and the landform is valley plain composed of class II and VII terraces of the Yellow River. Quwajiasi landslide is located in an erosion area where the Yellow River is strongly incised. The valley in the study area forms a canyon with high and steep slopes composed of Neogene mudstone on both sides. The top is covered with pebbles and loess like the soil accumulated in the high terrace of the Quaternary Yellow River. Quaternary alluvial proluvial silt, pebbles, broken stone soil, and silty clay are also distributed in the area. The study area is located in the southeastern Lajia basin. Due to the extrusion of adjacent tectonic units and the influence of later tectonic movement, the NW-SE Maqin-Maqu fault is visible. The iron fault (F1) developed on the north side of the Quwajiasi landslide is a branch fault of the Maqin fault, which is a compressive torsional reverse fault with an attitude of  $297^{\circ}\angle67^{\circ}-10^{\circ}\angle76^{\circ}$ , and the width of the fault fracture zone is 10–30 m. The study area has a typical plateau continental climate. Due to the invasion of humid airflow in the southwest and southeast, the climate is semihumid to alpine. Precipitation is small and uneven, evaporation is large, and the multiyear average temperature in the area is  $-0.1^{\circ}\text{C}$ . The average annual precipitation is 420–560 mm, the maximum daily rainfall is 40.6 mm, and the maximum hourly rainfall is 21.0 mm. The seismic peak acceleration in the study area is 0.15 g, and the basic seismic intensity is VII.

Weak layered mudstone is exposed in the study area, with a thickness of 0.05–0.1 m, inclined to the northeast at an inclination of  $5^{\circ}$ – $12^{\circ}$ . The groundwater in the study area is divided into two types: clastic rock pore fissure water and loose rock pore water. As shown in Figure 2, based on the landform characteristics and the relationship between deformation and failure, the landslide is divided into 7 engineering geological zones. The Quwajiasi landslide trends NE-SW, with the main sliding direction of  $298^{\circ}$ – $307^{\circ}$ . The landslide is 700–900 m long and 2500 m wide, the height

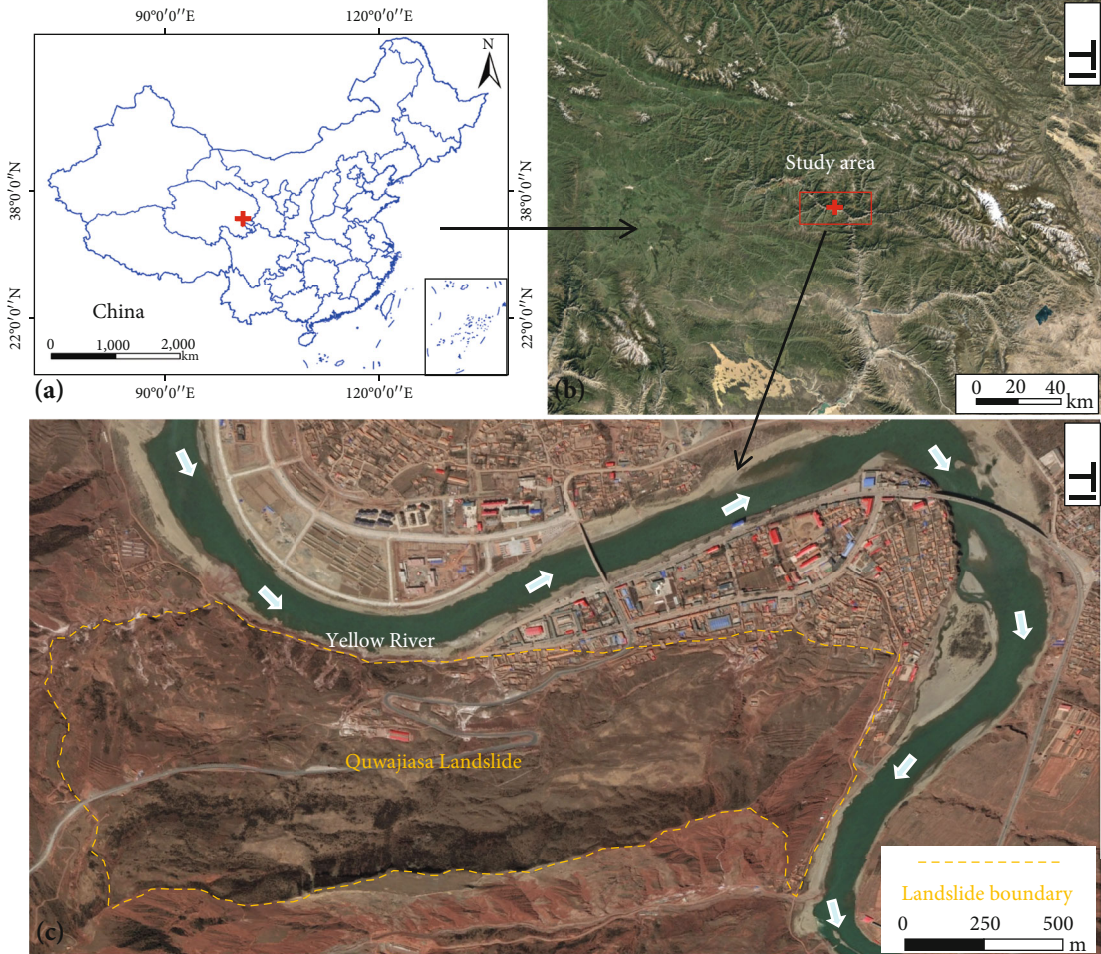


FIGURE 1: Location and topography of the study area.

difference between the front and rear edges ranges from 185 to 300 m, the slope is 25°–36°, and the total volume can reach  $1.67 \times 10^8 \text{ m}^3$ , making this a giant ancient landslide. The main failure mode of the Quwajiasa landslide is traction tension failure. The front slope is seriously deformed, forming large-scale shallow surface sliding failure with a continuous armchair shaped steep wall. The surface soil is seriously damaged and disintegrated. The central platform forms a multilevel parallel downward dislocation with well-developed tension fractures with a fracture width of 20–30 cm and downward dislocation of 0.3–2 m. A series of vertical cracks are developed along the rear part of the slope. The antislide pile beside the highway is deformed and damaged, the joint between the antislide pile and the sheet wall is sheared, deformed, and cracked, and the front of the pile is cracked and deformed and tilts out of the slope.

### 3. Data and Methods

**3.1. Small Baseline Subset Interferometric Synthetic Aperture Radar (SBAS-InSAR).** In this study, the Small Baseline Subsets Interferometric Synthetic Aperture Radar (SBAS-InSAR) method is adopted. Its basic principle is to first register images within a scene to the main image and then filter

and unwrap the obtained interferogram by setting the temporal and spatial baseline threshold. Coherence information is used to select highly coherent pixels in the unwrapping results. Then, after removing the elevation error phase and atmospheric delay phase in the difference map, the average deformation rate is obtained using singular value decomposition. Finally, the law of slow deformation of the surface with time is obtained. This method is suitable for mountainous areas with fewer buildings and fewer permanent scattering points.

This study uses Sentinel-1A satellite image data for SBAS-InSAR analysis. The Sentinel-1A satellite is a radar satellite launched by the European Space Agency in April 2014 with a cycle of 12 days. Satellite image data since October 2014 can be obtained on the official ESA website. The data coverage and monitoring scope are shown in Figure 3. The satellite has four imaging modes, EW, SM, IW, and wave. The SM mode and IW mode adopt the latest top imaging technology, which can address the scaling effect during wide range imaging and enhance imaging radiance. Sentinel-1 is equipped with a new generation C-band synthetic aperture radar system, which has a shorter wavelength than L-band. The main parameters of data image are shown in Table 1.

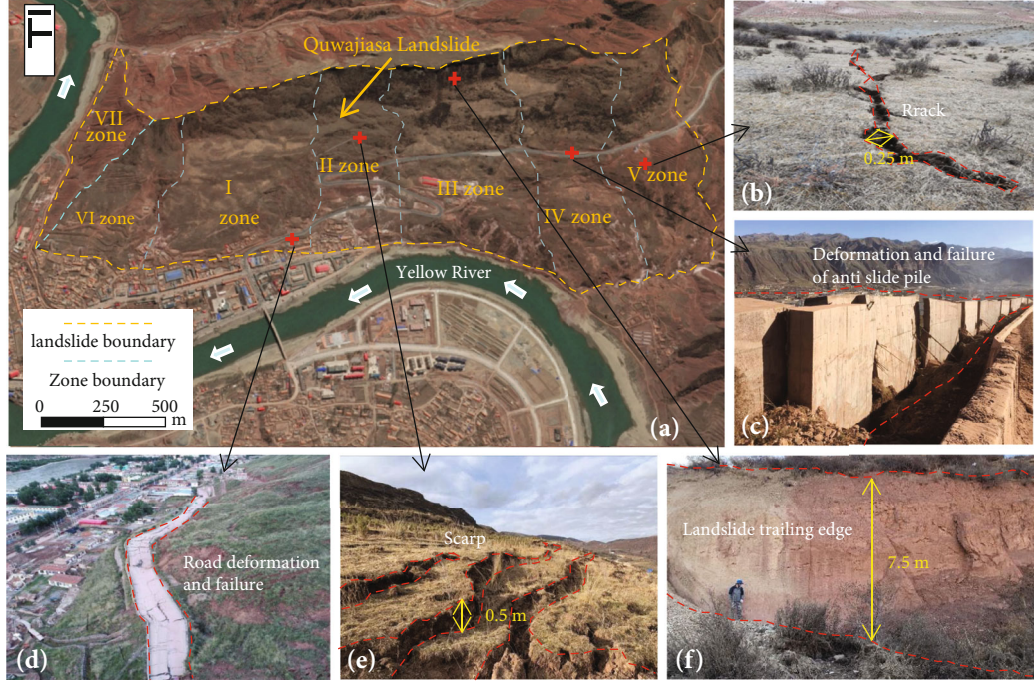


FIGURE 2: (a) Engineering geological zones of landslide. (b) Intermediate crack. (c) Deformation of anti slide pile. (d) The deformation of the path. (e) Central scarp. (f) Landslide trailing edge.

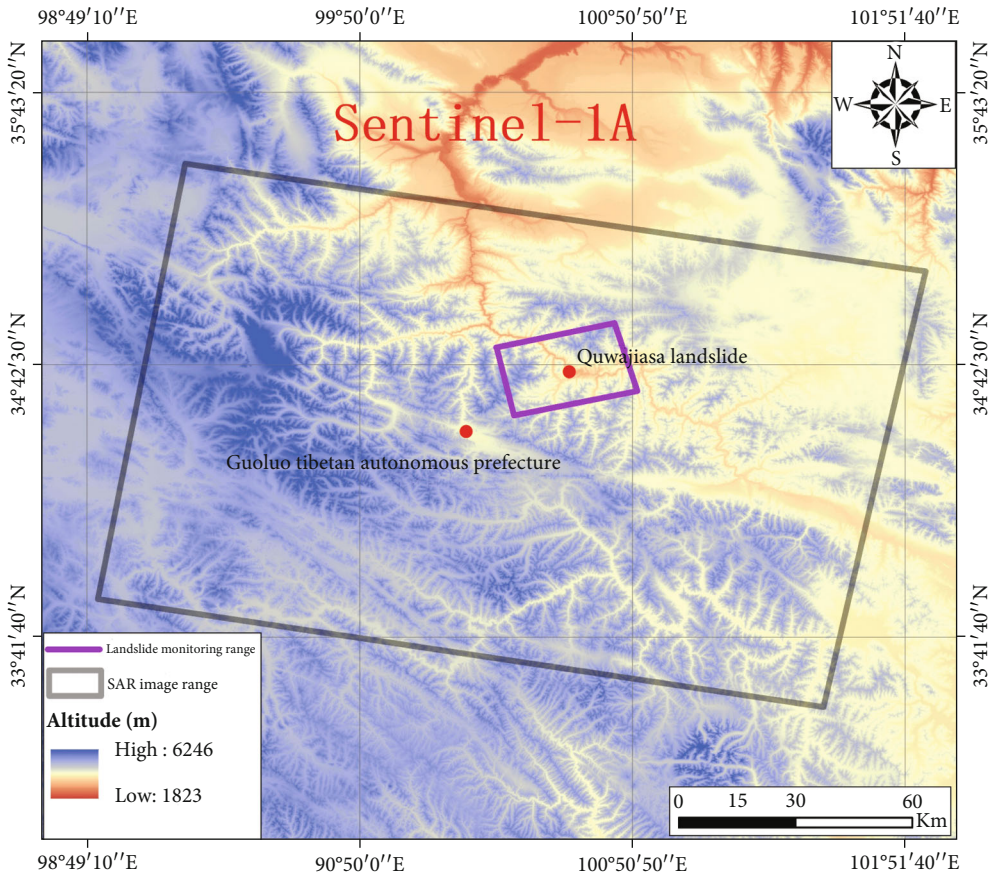


FIGURE 3: Data coverage and monitoring scope.

TABLE 1: Main parameters of data image.

Index	Flight platform	Flight direction	Imaging mode	Polarization mode	Resolving power	Wavelength	Coverage period
Parameter information	Sentinel-1A	Orbit lowering	IW	VV	5 m × 20 m	5.63 cm	2017.3.25-2020.6.25

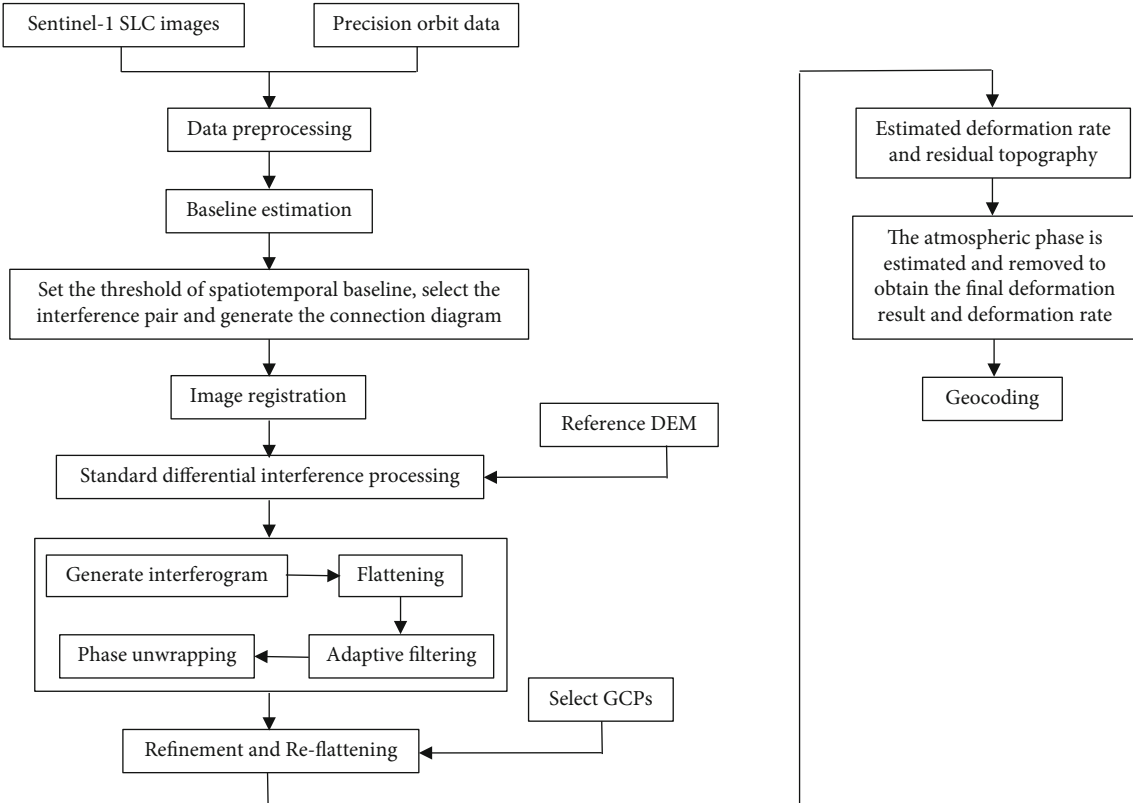


FIGURE 4: Data processing flow.

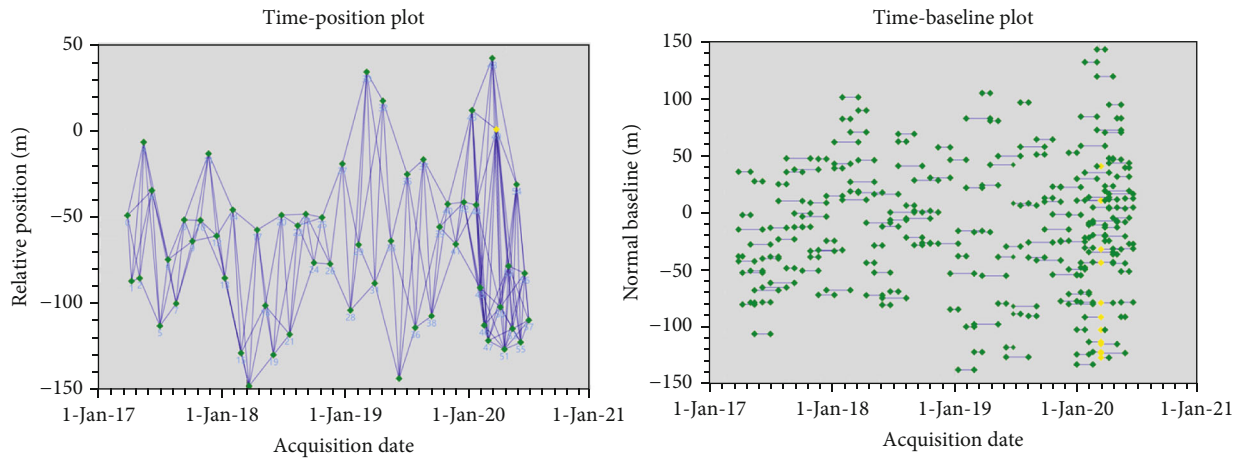


FIGURE 5: Spatial baseline (a) and temporal baseline (b).

This study uses the SBAS module in ENVI SARscape software to process the SAR data. As shown in Figure 4, SBAS technology primarily includes the generation of con-

nnection diagrams (the parameter settings of spatial baseline and temporal baseline are shown in Figure 5), the generation of interferograms, flattening interferograms, adaptive

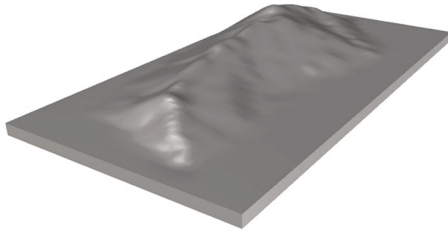


FIGURE 6: 3D calculation model diagram.

filtering, phase unwrapping, orbit refining and flattening, phase to deformation, and geocoding.

### 3.2. Numerical Simulation

**3.2.1. Establishment of the Calculation Model.** Midas is a finite element analysis software for structural design, which is divided into four categories: architecture, bridge, geotechnical, and simulation. This study primarily uses the Midas geotechnical module. In this modeling, the Midas software is used to establish the landslide model. As shown in Figure 6, the calculation range is 361 m high in the Z direction, the X axis runs along the front edge of the slope, the model length is 3930 m, the vertical slope outward is the Y axis, the model width is 2037 m, the model bottom elevation is 0 m, and the elevation of the highest point at the rear edge of the model is 361 m. As shown in Figure 7, according to the engineering geological profile in the area, there are two potential sliding surfaces, deep sliding surface 1 and deep sliding surface 2. The gravelly soil, silty clay, and clay on the upper part of the sliding surface are combined and classified as overburden. The parameters are determined by a combination of test results, empirical data, and inverse analysis [4, 25].

**3.2.2. Selection of Calculation Parameters.** The parameters of interest are bulk modulus  $K$  and shear modulus  $G$  [26]. As shown in Formula (1), the bulk modulus  $K$  and shear modulus  $G$  are converted by Poisson's ratio and elastic modulus. The selection of other rock and soil parameters is shown in Tables 2 and 3.

$$K = \frac{E_0}{3(1 - 2\mu)} \quad G = \frac{E_0}{2(1 + \mu)}. \quad (1)$$

**3.2.3. Computing Method.** The Mohr Coulomb (M-C) constitutive model is adopted in this calculation, and the strength reduction method is used to determine the stability coefficient of the specified sliding surface of the slope. The safety factor of slope stability in the strength reduction method is defined as the degree of shear strength reduction of the rock and soil mass when the slope reaches the critical failure state. The safety factor is defined as the ratio of the actual shear strength of the rock and soil mass to the reduced shear strength at critical failure. The key point of the strength reduction method is the formula:

$$\begin{aligned} C_F &= C/F, \\ \varphi_F &= \tan^{-1}((\tan \varphi)/F). \end{aligned} \quad (2)$$

To adjust the strength index  $C$  and  $\varphi$ , then the slope stability numerical analysis is carried out. By continuously increasing the reduction coefficient and repeatedly calculating until it reaches critical failure, the reduction coefficient obtained at this time is the safety factor  $F$ .

**3.3. Combination Methodology.** The first part of this study is the field investigation, which primarily determines the engineering geological conditions of the Quwajiasa landslide. Based on the landform and relationship between deformation and failure, the landslide is divided into zones, and the failure mode of landslide is analyzed. In addition, a detailed investigation was conducted inside the landslide to determine the local deformation and location of the landslide, such as shallow surface sliding, scarp, soil disintegration, tension cracks, and small landslide. Then, the whole deformation rate of the Quwajiasa landslide mass is obtained via InSAR interpretation, and the areas with significant deformation and no significant deformation were identified. For the strong deformation region, the time series deformation cumulative curve of feature points is extracted, and its deformation characteristics are analyzed. Finally, using FLAC3D numerical simulation, the stability coefficient of the landslide is determined using the strength reduction method, the stability coefficients of the two sliding surfaces are calculated, and the deformation law of the landslide is analyzed. The joint use of the three methods allows for comparison and confirmation of the field investigation and InSAR monitoring results, and InSAR monitoring results and FLAC3D simulation results ensure the accuracy of the calculation. Compare the local deformation of the landslide and small landslide in the field investigation with the position of strong deformation area monitored by InSAR as well as recheck the InSAR monitoring results with the field investigation. Then, the deformation monitored using InSAR is compared with the FLAC3D simulation results to determine the control relationship between the two deep sliding surfaces and the landslide deformation.

## 4. Results

### 4.1. InSAR Monitoring Results and Deformation Analysis

**4.1.1. Overall Deformation Monitoring Results of Landslide.** As shown in Figure 8, InSAR interpretation results show that the maximum surface deformation rate of the Quwajiasa landslide mass (black solid line range) can reach -70 mm/y, and the overall deformation rate is -70–7 mm/y. There are clear deformation signs from area I to area V overall, and there are no significant deformation signs in areas VI and VII. The slope deformation within the red dotted line is the strongest (areas A and B). The deformation rate is -70 –35 mm/y. The significant deformation area in area A is 0.1 km<sup>2</sup>, and the significant deformation area in area B is 0.33 km<sup>2</sup>. As shown in Figure 8, the black arrow is the possible sliding direction of the deformation area. In the case of a landslide disaster, local village roads are under direct threat (according to the radar side imaging characteristics, the positive value of the rate represents that the azimuth of surface

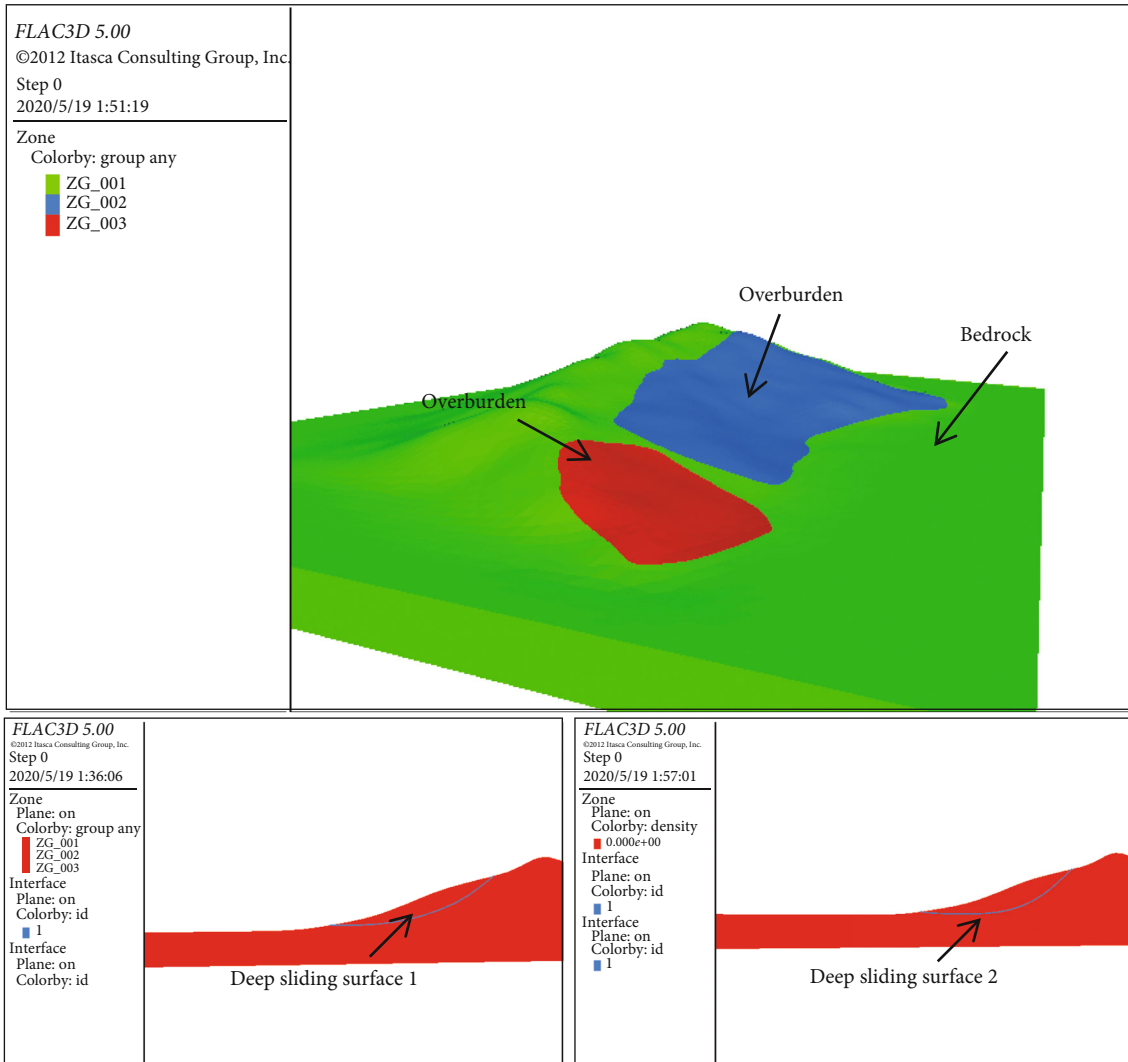


FIGURE 7: FLAC calculation model diagram.

TABLE 2: Model parameter value table.

Rock and soil type	Bulk density (natural) $\gamma$ (KN/m <sup>3</sup> )	Cohesion (natural) (c/KPa)	Internal friction angle (natural) ( $\varphi/\circ$ )	Bulk modulus (K/pa)	Shear modulus (G/pa)
Overburden	19.9	19.9	17.9	$4.6 \times 10^8$	$2.3 \times 10^8$
Mudstone	21	690	35.2	$8.1 \times 10^9$	$6 \times 10^9$

TABLE 3: Parameter value of sliding surface.

Slip surface type	Cohesion (natural) (c/KPa)	Internal friction (natural) angle ( $\varphi/\circ$ )	Normal stiffness (KS/pa)	Tangential stiffness (KN/pa)
Deep sliding surface 1	23.5	19.8	$4.6 \times 108$	$2.3 \times 108$
Deep sliding surface 2	32.5	25.1	$6.6 \times 108$	$4.3 \times 108$

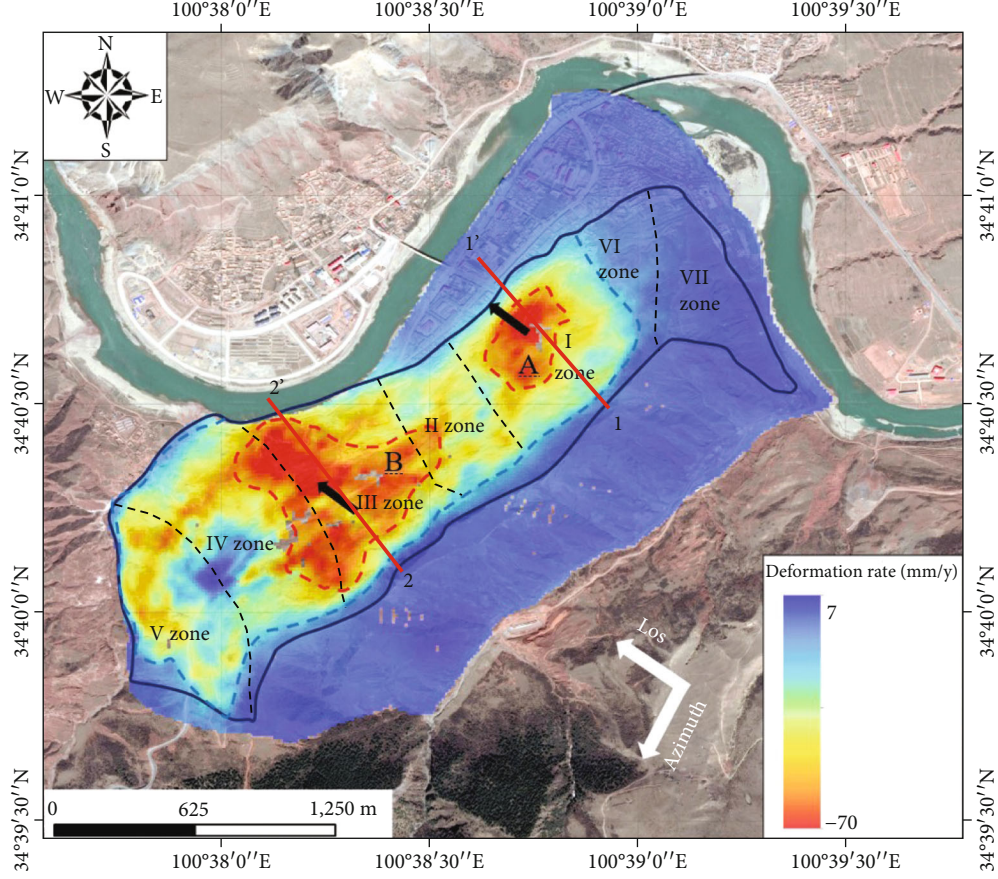


FIGURE 8: The annual average rate of deformation of the Quwajiasi landslide.

movement is close to the satellite shooting azimuth, and the negative value represents that the azimuth of surface movement is far away from the satellite shooting azimuth; there are no clear deformation signs in other areas outside the blue dotted line, and the slope surface is relatively stable in this time period).

**4.1.2. Deformation Analysis of the Strong Deformation Zone.** The overall deformation rate of zone I is  $-70\text{--}7\text{ mm/y}$ . Using InSAR technology, the surface deformation information of I area in different years is extracted. The deformation rate of 1-1' section in I area is shown in Figure 9. During the monitoring period from March 2017 to June 2020, the fluctuation of the deformation rate curve of section I in 2018 was the strongest, indicating that significant deformation occurred on the slope surface during this period. During the monitoring period from January to June in 2020, the change in the section deformation rate curve in zone I was relatively stable compared to previous years, and the deformation rate magnitude was small, indicating that the deformation of the slope body in zone I was weak in this period. The deformation rate curves of 2017 and 2019 are consistent, and the deformation magnitude is less than that of 2018 as well as greater than that from January to June 2020.

The slope in zone III is in a state of strong deformation, and the maximum deformation rate can reach  $-70\text{ mm/y}$ ,

which is the area with the widest distribution of strong deformation and largest deformation rate. Using InSAR technology, the section deformation rate in different years was extracted for zone III. The 2-2' deformation rate profile of zone III is shown in Figure 9. The interruption of the profile deformation rate curve indicates that there is a decoherence in the slope body during InSAR monitoring, and no deformation information is available. During the monitoring period of 2017, the deformation rate of the middle of the landslide was the largest, followed by the deformation of the leading edge, and the deformation rate reached a maximum value of  $-60\text{ mm/y}$  near the ZK22 borehole location. During the monitoring period in 2018 and 2019, the deformation rate in the middle was the largest, and the deformation rate near the ZK23 drilling position reached a maximum value of  $-58\text{ mm/y}$  and  $-62\text{ mm/y}$ , respectively. During the monitoring period from January to June 2020, the maximum deformation rate reached  $-42\text{ mm/y}$ .

There is a strong deformation zone A in the middle and front of zone I, and the deformation rate of zone A is  $-70\text{--}35\text{ mm/y}$ , indicating moderate to strong deformation in zone I. The slope in zone A (within the range enclosed by the red circle) has a maximum line-of-sight deformation rate of  $-70\text{ mm/y}$ . The area is  $0.1\text{ km}^2$ , and the average slope is  $41^\circ$ . According to the radar side imaging characteristics, the slope in area A is roughly interpreted to be moving to

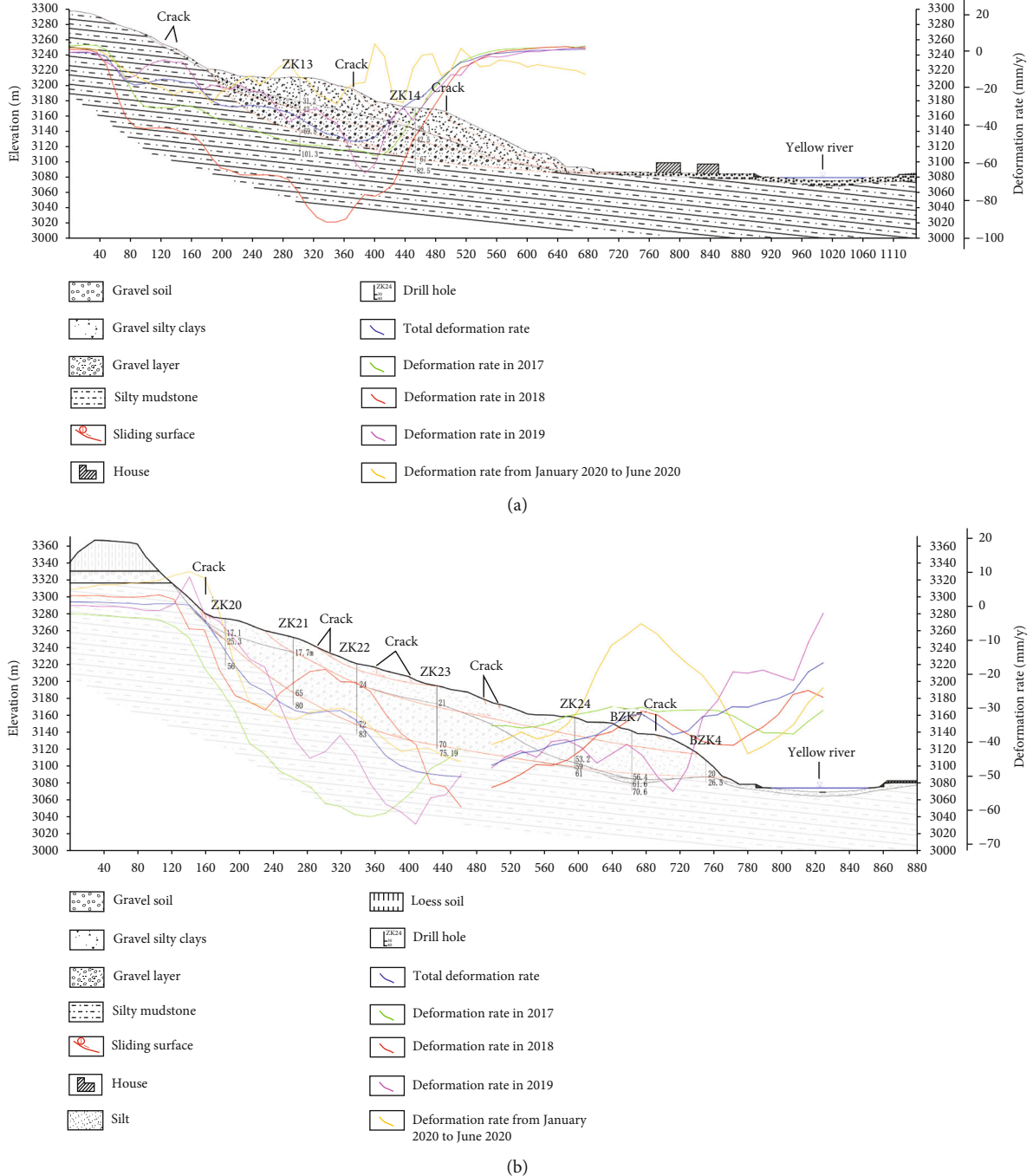


FIGURE 9: (a) 1-1' InSAR deformation profile. (b) 2-2' InSAR deformation profile.

the northwest, as shown by the black arrow in Figure 10. As shown in Figure 10, in order to analyze the time-series change characteristics of the strong deformation area in area A, three feature points of the trailing edge P1, middle P2, and leading edge P3 were extracted, and their deformation accumulation curves were drawn. The timing diagram shows that during the monitoring time from 20170325 to 20191216, the cumulative deformation value of point P3 is the largest (190 mm), the cumulative deformation value of point P2 is the second largest (180 mm), and the cumulative

deformation value of point P1 is the smallest. In terms of deformation trend, the deformation of the leading edge of the slope in area A > the deformation of the middle part > the deformation of the trailing edge and the deformation characteristics are similar to the local traction sliding deformation.

The strong deformation zone B spans zone II, zone III, and zone IV. The maximum line-of-sight deformation rate of zone B can reach -70 mm/y. The area of this deformation zone is 0.43 km<sup>2</sup>, the altitude distribution ranges from 3085

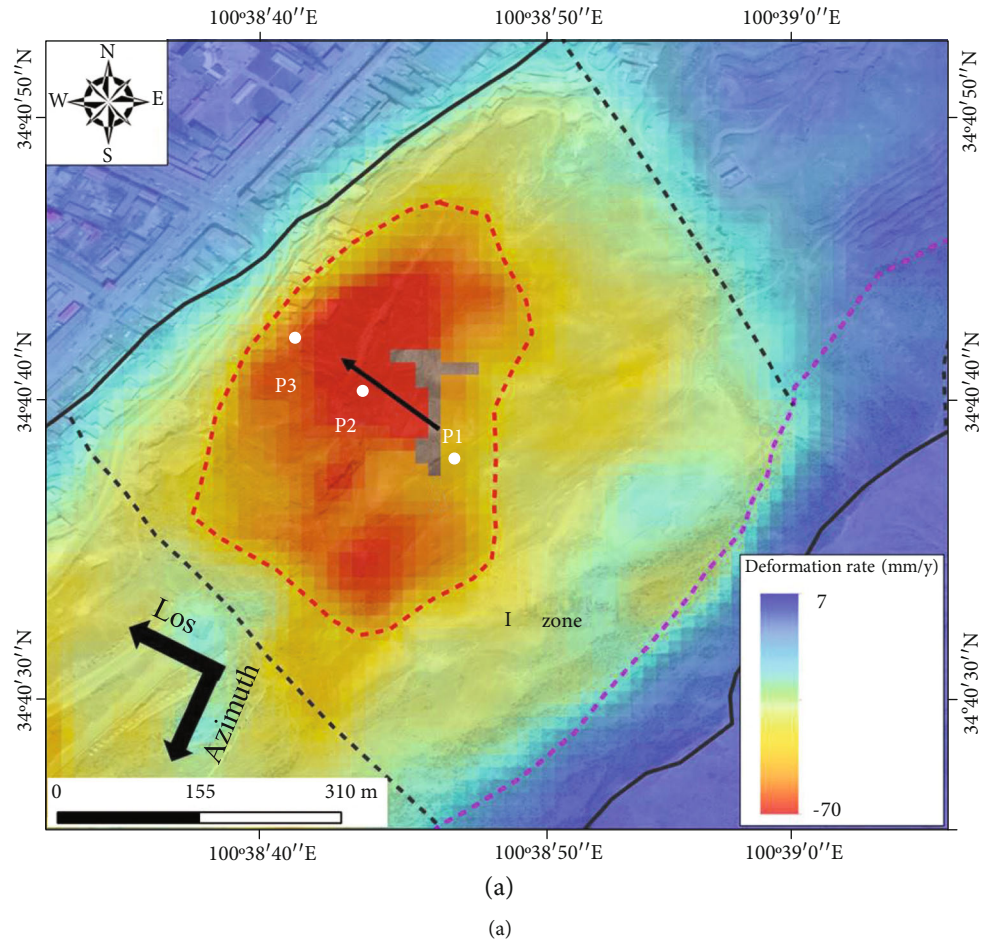


FIGURE 10: Continued.

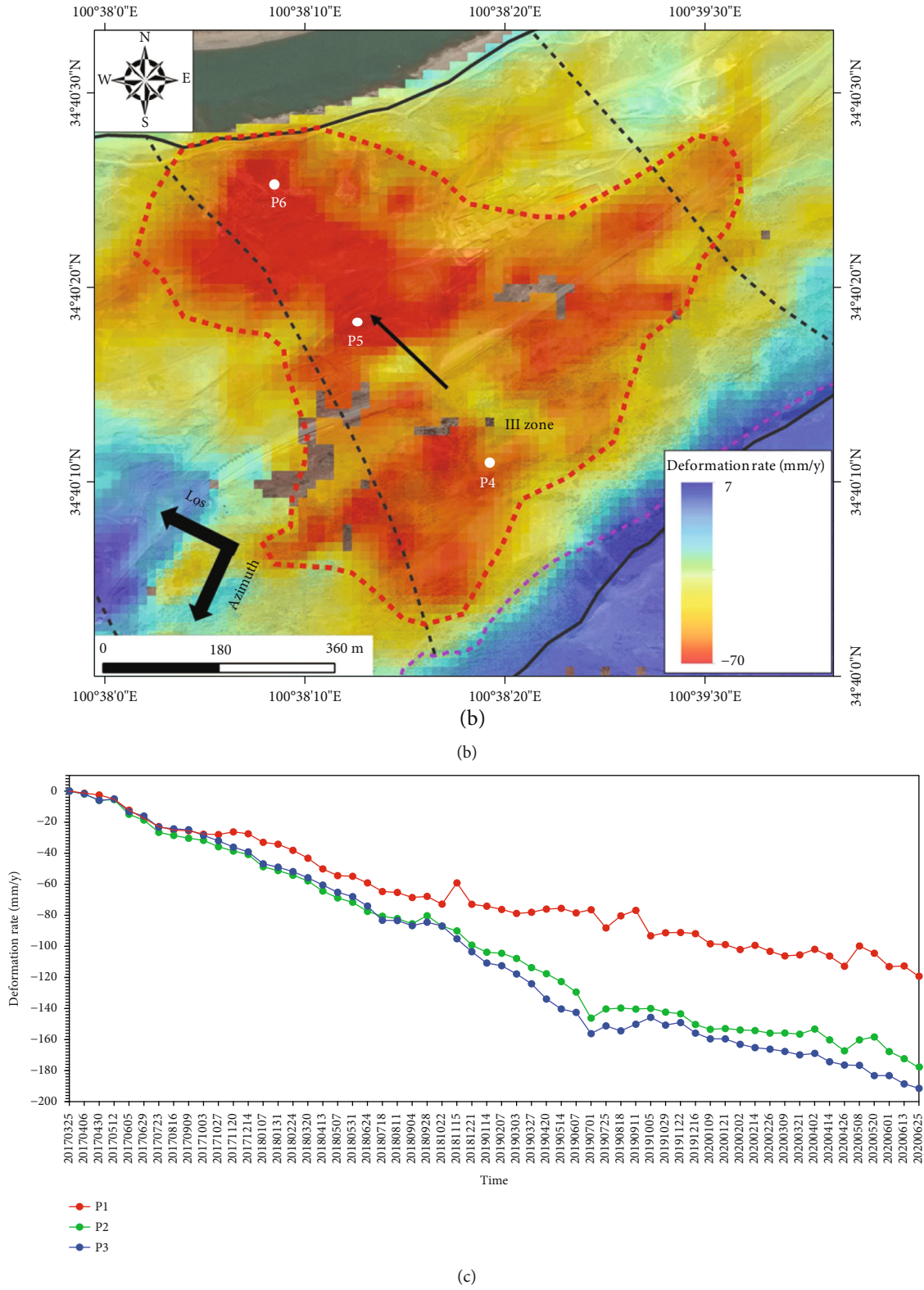
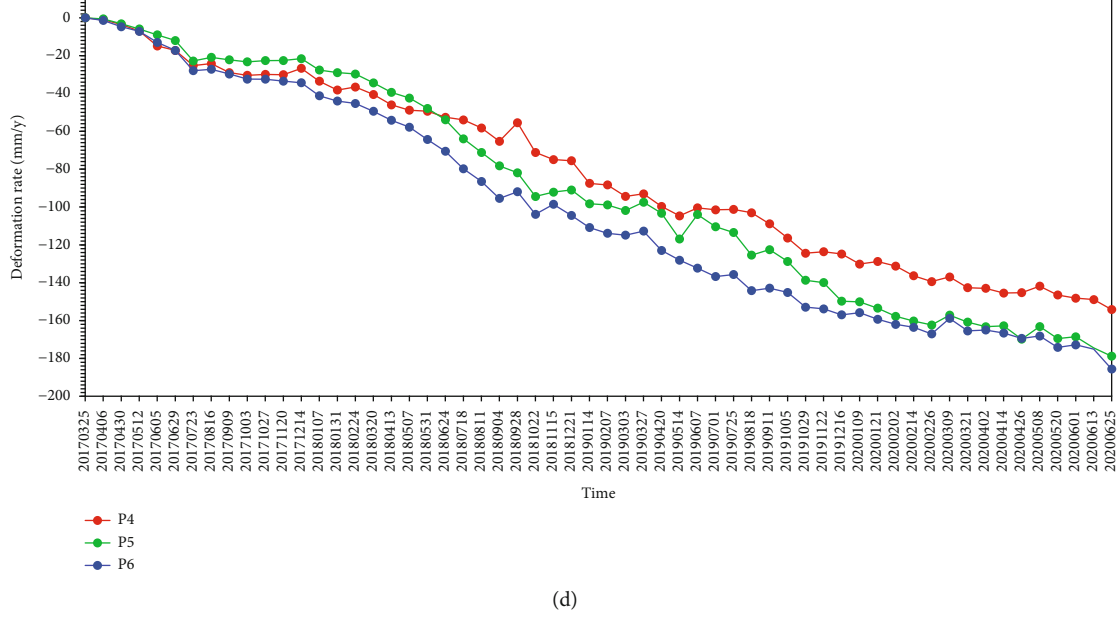


FIGURE 10: Continued.



(d)

FIGURE 10: (a) The average annual deformation rate distribution of strong deformation zone A (2017.3-2020.6). (b) The average annual deformation rate distribution of strong deformation zone B (2017.3-2020.6). (c) Time series deformation diagram of characteristic point A in strong deformation zone. (d) Time series deformation diagram of characteristic point B in strong deformation zone.

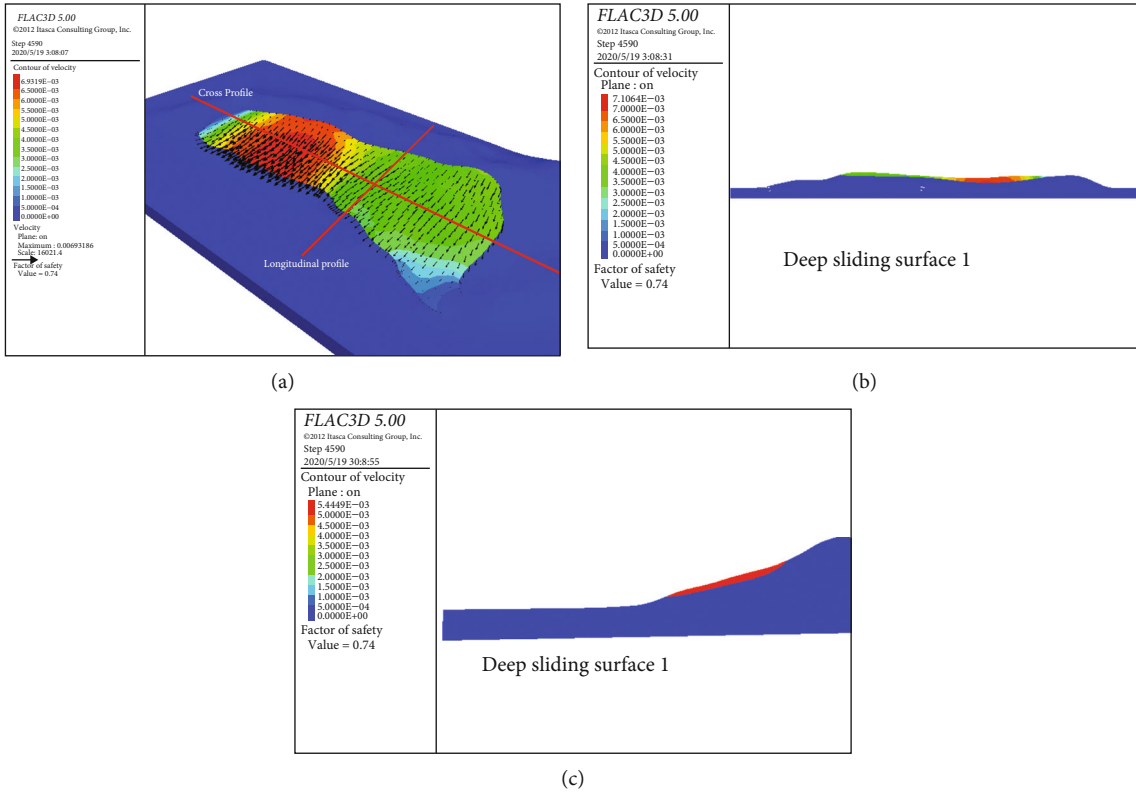


FIGURE 11: (a) Stability calculation results of deep sliding surface 1 (I-IV) under seismic conditions. (b) Stability calculation results of deep sliding surface 1 (I-IV) under seismic conditions (crossprofile). (c) Stability calculation results of deep sliding surface 1 (I-IV) under seismic conditions (longitudinal profile).

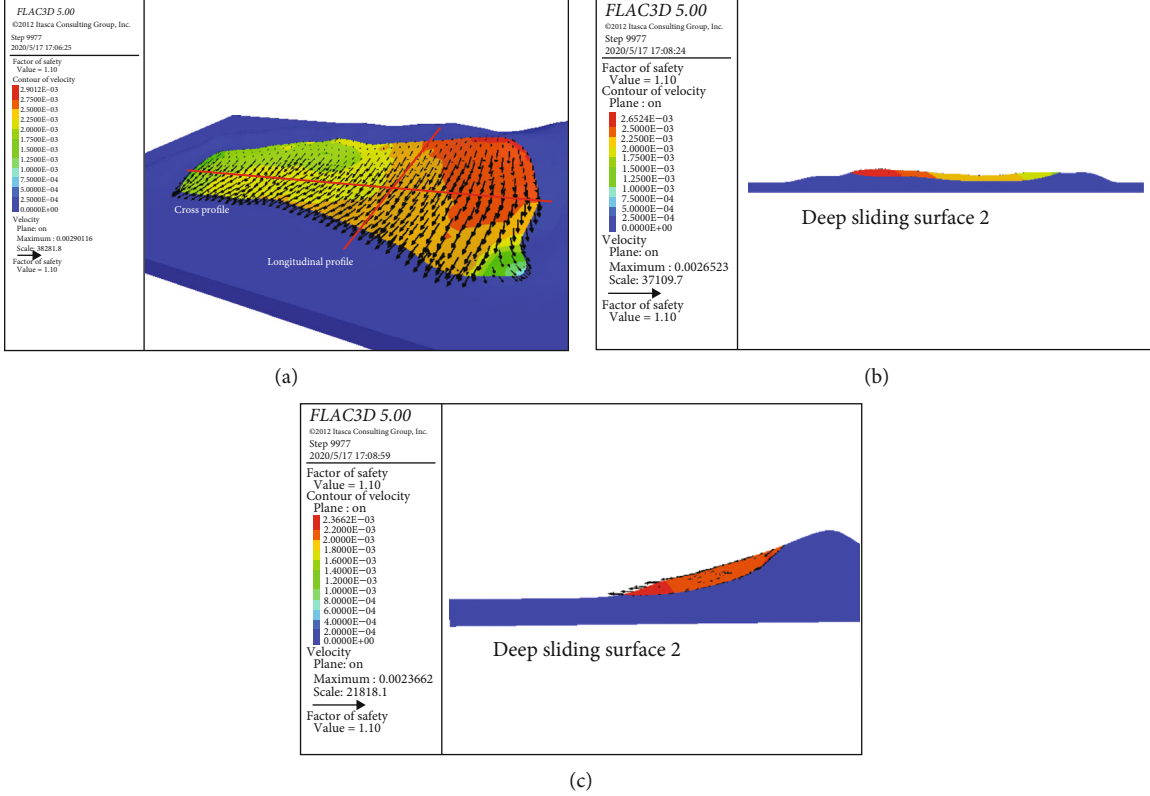


FIGURE 12: (a) Stability calculation results of deep sliding surface 2 (I-IV) under seismic conditions. (b) Stability calculation results of deep sliding surface 2 (I-IV) under seismic conditions (crossprofile). (c) Stability calculation results of deep sliding surface 2 (I-IV) under seismic conditions (longitudinal profile).

to 3325 m, and the height difference is 240 m. The slope inclination is 18°–25°, the leading edge is steeper, the middle is gentler, and the trailing edge is steeper. Artificially excavated roads along the leading edge and middle as well as human engineering activities are clearly visible. According to the radar side imaging characteristics, the slope in area A is roughly interpreted to be moving to the northwest, as shown by the black arrow in Figure 10. As shown in Figure 10, in order to analyze the time-series change characteristics of the slope in area B, three characteristic points on the trailing edge P4, middle P5, and leading edge P6 were extracted, and the cumulative deformation curve was drawn, as shown in Figure 10. The time series diagram shows that during the monitoring time from 20170325 to 20200625, the cumulative deformation variables of each feature point are different but have a similar trend. The cumulative deformation of point P6 is the largest (185 mm); the cumulative deformation of point P5 is the second largest (178 mm); the cumulative deformation of point P4 is the smallest (154 mm). Clearly visible deformation features are visible across the overall slope. The cumulative deformation of the three feature points continued to increase from March 2017 to June 2020, among which the deformation of P6 feature point increased the fastest. The increase rate of P4 feature point deformation was slower than that of P5. Comprehensive analysis shows that the overall deformation characteristics of the slope in area B are similar to the local traction sliding deformation.

**4.2. Numerical Simulation Results.** A seismic acceleration of 0.15 g in the horizontal direction is added to the model. On this basis, the strength reduction method is used to determine the slope stability coefficient. Results show that the stability coefficient of the deep sliding surface 1 of the slope (areas I-IV) is 0.74, and the stability coefficient of deep sliding surface 2 is 1.10 for the overall deformation. Under seismic conditions, the deep sliding surface 1 of the slope is in an unstable state, and the deep sliding surface 2 is stable.

As shown in Figure 11, results of sliding surface 1 show that the maximum displacement of the landslide appears on the right side of the landslide. In general, the high value area of displacement is also primarily concentrated on the right side of the landslide. The displacement distribution in the main sliding direction ( $X$  direction) is generally consistent with the overall displacement distribution, and the displacement in the  $Y$  direction and  $Z$  direction is small. Displacement of the leading edge on the right side of the landslide is large, indicating that the leading edge on the right side of the landslide has undergone significant deformation.

As shown in Figure 12, results of sliding surface 2 show that the maximum displacement of the landslide appears on the left side of the landslide. In general, the high value area of displacement is also primarily concentrated on the left side of the landslide. The displacement distribution in the main sliding direction ( $X$  direction) is generally consistent with the overall displacement distribution, and the displacement in the  $Y$  and  $Z$  directions is small. The displacement of the

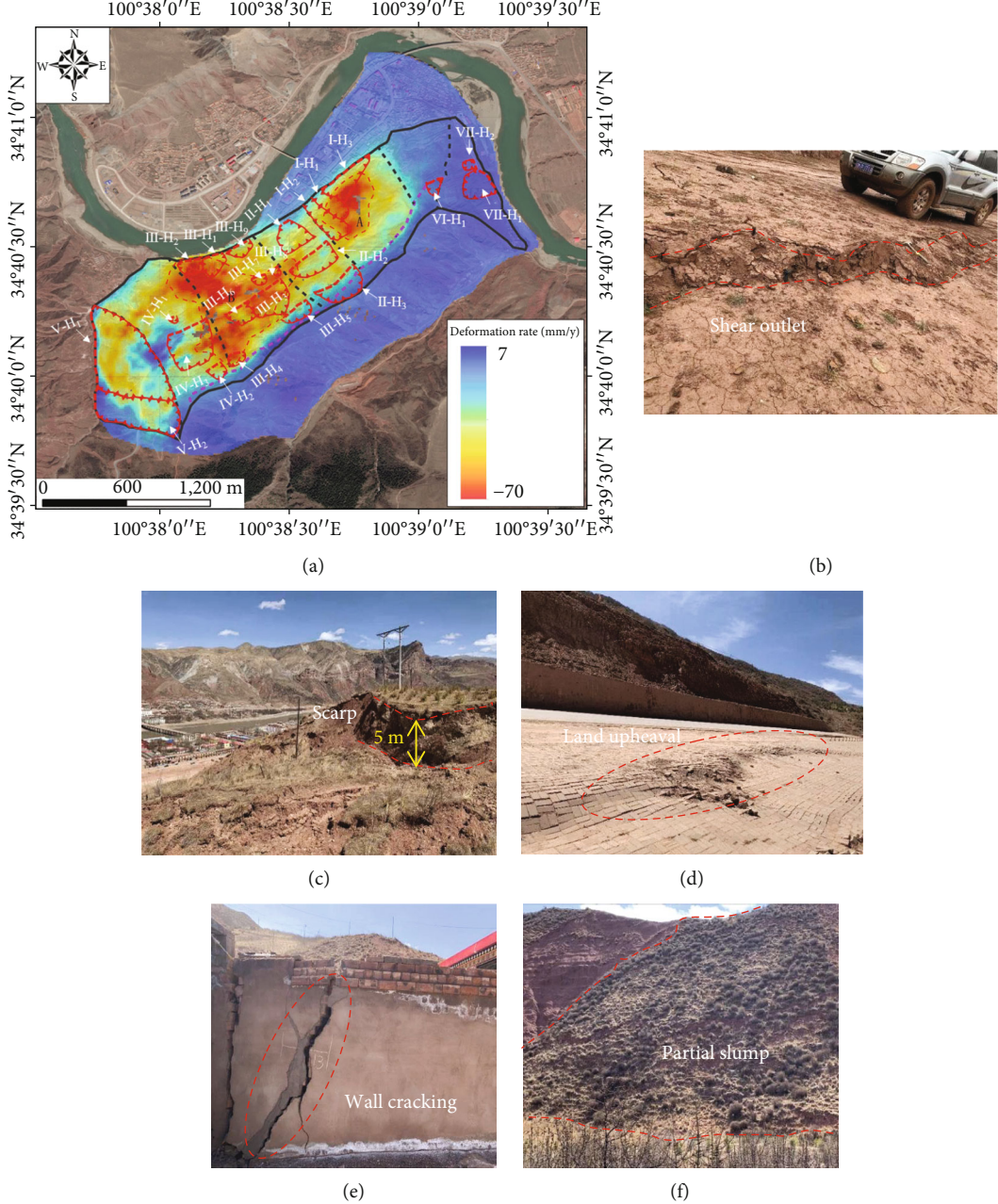


FIGURE 13: (a) Comparison and verification diagram of InSAR interpretation and field survey. (b) Front shear outlet. (c) Front steep wall. (d) Ground uplift of the viewing platform. (e) Building deformation. (f) Partial slump.

left trailing edge of the landslide is large, indicating that the left trailing edge of the landslide has undergone significant deformation and gradually decreases to the leading edge of the landslide.

## 5. Discussion

From the InSAR results, the deformation characteristics of zone I in different years from March 2017 to June 2020 are as follows: central deformation > leading edge deformation > trailing edge deformation. For the total deformation, the fluctuation of deformation rate in the middle is the largest,

and the maximum value of deformation variable can reach -55 mm/y. The leading edge shape variable is the second largest, and the trailing edge shape variable is the smallest. The slope in zone I shows traction sliding deformation overall. According to the field investigation results, the highway excavation slope and local residents' slope cutting and building houses in area I form free surfaces of varying heights, which provides space for shear deformation of the landslide. Local sliding failure occurred on the inner side of the highway in area I. A free surface I formed again at the rear edge of the small landslide, and the tension deformation of the top platform at the rear edge begins to occur under traction

deformation due to the weight of the landslide. The overall performance is also traction sliding deformation [27], which is consistent with the InSAR monitoring results.

From the change trend of the InSAR curve in zone III, the deformation rate characteristics of the general section are as follows: the deformation rate of the middle part is the largest, the deformation rate of the leading edge is the second largest and gradually weakens as the slide slows down, and the deformation rate of the trailing edge is the smallest. Comprehensive analysis shows that the slope in zone III is traction sliding deformation overall. According to the field investigation results, the erosion of the Yellow River on the bank slope forms a good front shear outlet [28], and human engineering excavation provides the spatial conditions for deformation of the landslide. After a free surface is formed again at the rear edge of the small landslide, tension deformation of the platform at the top of the rear edge begins to occur under traction deformation due to the weight of the landslide. The shallow surface of the front edge of this area is significantly slippery, and the slope surface disintegrates. Zone III belongs to the traction failure mode, which is consistent with InSAR monitoring results.

Using InSAR technology to monitor the Quwajiasi landslide, the surface of the slope body in areas I~V shows clear deformation signs, and the deformation rate is between -70 and -7 mm/y [29]. There are 2 strong deformation areas (A~B areas) and a total of 23 small landslides, and the overall distribution of landslides is shown in Figure 13. The 20 surveyed landslides are all within the significant deformation area monitored by InSAR, and the deformation rate of the remaining 3 landslides (VI-H<sub>1</sub>, VII-H<sub>1</sub>, VII-H<sub>2</sub>) is -7~7 mm/y. Compared with the overall landslide mass, there is no clear deformation signal, and the slope mass is relatively stable. Strong deformation zone A is located in the middle and front of zone I, and the middle and trailing edges of landslides I-H<sub>1</sub> to I-H<sub>3</sub> are all located in zone A, indicating that the deformation of the trailing edge of the landslides at I-H<sub>1</sub> to I-H<sub>3</sub> is greater than the deformation of the leading edge. The deformation range of area A continues to expand upward to 4018 m above sea level along the trailing edge of 3 landslides I-H<sub>1</sub>~I-H<sub>3</sub>. The strong deformation area B has a wider distribution range, and the deformation area extends from 4016 m above sea level to 4025 m above sea level. Seven landslides H<sub>1</sub>-III-H<sub>4</sub> ad III-H<sub>6</sub>-III-H<sub>8</sub> are located in the strong deformation area of B area; the other 10 landslides (II-H<sub>1</sub>-II-H<sub>3</sub>, III-H<sub>5</sub>, III-H<sub>9</sub>, IV-H<sub>1</sub>-IV-H<sub>3</sub>, V-H<sub>1</sub>-V-H<sub>2</sub>) are not within the strong deformation zones A or B; although, they still show clearly deformation signals. The deformation rates of these 10 landslides are less than those of A and B zones.

Comparing the monitoring results of InSAR with the results of numerical simulation, the numerical simulation results for sliding surface 1 show that the high value area of landslide displacement is concentrated on the right side of the landslide, which is the same as the location of strong deformation area A from the InSAR monitoring results, and the range of high value area of displacement is roughly the same as that of strong deformation area A. The numerical simulation results for slip surface 2 show that the high

value area of landslide displacement is concentrated on the left side of the landslide, which is the same as the location of strong deformation area B from the InSAR monitoring results, and the range of high value area of displacement is roughly the same as that of strong deformation area B. However, there is no strong deformation area on the left side of the landslide in the numerical simulation results for sliding surface 1, and there is no strong deformation area on the right side of the landslide in the numerical simulation results for sliding surface 2. To summarize, the deformation and stability of the right side of the Quwajiasi landslide are controlled by sliding surface 1, and the deformation and stability of the left side are controlled by sliding surface 2 [30]. Numerical simulation results show that the high displacement area of the landslide is concentrated on the left and right sides of the landslide, which is the same as the strong deformation areas A and B from the InSAR data. The main controlling factors of strong deformation area A are the construction of provincial road excavation slopes and local slope cutting and house construction by residents, forming free surfaces with different heights. The main controlling factor of strong deformation area B is undercutting of the Yellow River, which makes the front edge of the area free, providing better conditions for landslide cutting [21].

## 6. Conclusions

The main purpose of this paper is to study the deformation and stability analysis of a multislip surface large-scale loess landslide in the Yellow River Basin from the perspective of field investigation, InSAR monitoring, and numerical simulation. First, a field investigation was conducted to determine the lithology and structure of the study area as well as carry out engineering geological zoning according to the deformation and failure characteristics of the landslide. Through InSAR monitoring and analysis of the deformation history of the landslide, the strong, weak, and abnormal deformation areas were identified and compared with the field investigation results. Finally, the overall stability of the landslide was evaluated through numerical simulation. The primary conclusions of this study are as follows:

- (1) The landslide is divided into seven engineering geological zones, of which zones I to V have clear deformation signs overall, and zones VI and VII show no significant deformation
- (2) InSAR monitoring results show that strong deformation area A is located in area I, and area B spans areas II, III, and IV, which shows local traction sliding deformation
- (3) Numerical simulation results show that the deep sliding surface 1 of the landslide is in an unstable state, and the deep sliding surface 2 is in a stable state. By comparing the deformation characteristics of numerical simulation with field investigation and InSAR results, it is found that the deformation and stability of zone I are primarily controlled by deep sliding surface 1, and the deformation and stability

- of zones II, III, and IV are primarily controlled by the deep sliding surface 2
- (4) In this study, a deformation analysis and stability evaluation of a large-scale loess landslide with multiple slip surfaces in the Yellow River Basin were conducted using InSAR, numerical simulation, and traditional field investigation. The treatment process should focus on the strong deformation areas A and B. The results are useful for disaster prevention and reduction of loess disasters in the Yellow River Basin

## Data Availability

The data are available and explained in this article; readers can access the data supporting the conclusions of this study.

## Disclosure

I would like to declare on behalf of my co-authors that the work described is original research and has not been previously published.

## Conflicts of Interest

The authors declare no conflict of interest.

## Authors' Contributions

The manuscript is approved by all authors for publication.

## Acknowledgments

The author thanks the project supported by the Department of Natural Resources of Qinghai Province. We thank the editor and anonymous reviewers for improving the original manuscript.

## References

- [1] J. Peng, S. Wang, Q. Wang et al., "Distribution and genetic types of loess landslides in China," *Journal of Asian Earth Sciences*, vol. 170, pp. 329–350, 2019.
- [2] M. Pécsi, "Loess is not just the accumulation of dust," *Quaternary International*, vol. 7, pp. 1–21, 1990.
- [3] J. Zhuang, J. Peng, G. Wang, I. Javed, Y. Wang, and W. Li, "Distribution and characteristics of landslide in Loess Plateau: a case study in Shaanxi province," *Engineering Geology*, vol. 236, pp. 89–96, 2018.
- [4] X. S. Li, Q. H. Li, Y. J. Hu et al., "Study on three-dimensional dynamic stability of open-pit high slope under blasting vibration," *Lithosphere*, vol. 2021, no. Special 4, article 6426550, 2022.
- [5] J. Zhuang, J. Peng, X. Zhu, W. Li, P. Ma, and T. Liu, "Spatial distribution and susceptibility zoning of geohazards along the Silk Road, Xian-Lanzhou," *Environmental Earth Sciences*, vol. 75, no. 8, article 711, 2016.
- [6] Z. Dou, Y. M. Liu, X. Y. Zhang et al., "Influence of layer transition zone on rainfall-induced instability of multilayered slope," *Lithosphere*, vol. 2021, no. Special 4, article 2277284, 2021.
- [7] C. Meisina, F. Zucca, D. Fossati, M. Ceriani, and J. Allievi, "Ground deformation monitoring by using the Permanent Scatterers Technique: the example of the Oltrepo Pavese (Lombardia, Italy)," *Engineering Geology*, vol. 88, no. 3-4, pp. 240–259, 2006.
- [8] M. Necsoiu, R. N. McGinnis, and D. M. Hooper, "New insights on the Salmon Falls Creek Canyon landslide complex based on geomorphological analysis and multitemporal satellite InSAR techniques," *Landslides*, vol. 11, no. 6, pp. 1141–1153, 2014.
- [9] J. Wasowski and F. Bovenga, "Investigating landslides and unstable slopes with satellite multi temporal interferometry: current issues and future perspectives," *Engineering Geology*, vol. 174, pp. 103–138, 2014.
- [10] Y. Zhang, X. Meng, G. Chen, L. Qiao, R. Zeng, and J. Chang, "Detection of geohazards in the Bailong River Basin using synthetic aperture radar interferometry," *Landslides*, vol. 13, no. 5, pp. 1273–1284, 2016.
- [11] E. Intrieri, F. Raspini, A. Fumagalli et al., "The Maoxian landslide as seen from space: detecting precursors of failure with Sentinel-1 data," *Landslides*, vol. 15, no. 1, pp. 123–133, 2018.
- [12] M.-Z. Gao, B.-G. Yang, J. Xie et al., "The mechanism of micro-wave rock breaking and its potential application to rock-breaking technology in drilling," *Petroleum Science*, 2022.
- [13] C. Zhu, M. Karakus, M. C. He et al., "Volumetric deformation and damage evolution of Tibet interbedded skarn under multistage constant-amplitude-cyclic loading," *International Journal of Rock Mechanics and Mining Sciences*, vol. 152, article 105066, 2022.
- [14] Y. Zhang, X. Meng, C. Jordan, A. Novellino, T. Dijkstra, and G. Chen, "Investigating slow-moving landslides in the Zhouqu region of China using InSAR time series," *Landslides*, vol. 15, no. 7, pp. 1299–1315, 2018.
- [15] K. Zhu, P. Xu, C. Cao, L. Zheng, Y. Liu, and X. Dong, "Preliminary identification of geological hazards from Songpinggou to Feihong in Mao County along the Minjiang River using SBAS-InSAR technique integrated multiple spatial analysis methods," *Sustainability*, vol. 13, no. 3, p. 1017, 2021.
- [16] X. Liu, C. Zhao, Q. Zhang, Z. Lu, and F. Dai, "Investigating the Deformation History and Failure Mechanism of HEIFANGTAE Loess Landslide, China with Multi-Source SAR Data," in *In Proceedings of the IEEE International Geoscience and Remote Sensing Symposium (IGARSS)*, Yokohama, Japan, 2019.
- [17] C. Cao, W. Zhang, J. P. Chen, B. Shan, S. Y. Song, and J. W. Zhan, "Quantitative estimation of debris flow source materials by integrating multi-source data: a case study," *Engineering Geology*, vol. 291, article 106222, 2021.
- [18] B. Bayer, A. Simoni, D. Schmidt, and L. Bertello, "Using advanced InSAR techniques to monitor landslide deformations induced by tunneling in the Northern Apennines, Italy," *Engineering Geology*, vol. 226, pp. 20–32, 2017.
- [19] Y. Takada and G. Motono, "Spatiotemporal behavior of a large-scale landslide at Mt. Onnebetsu-dake, Japan, detected by three L-band SAR satellites," *Earth Planets and Space*, vol. 72, no. 1, 2020.
- [20] L. Wang, S. Wang, G. Li, and L. Wang, "Construction of 3D creep model of landslide slip-surface soil and secondary development based on FLAC3D," *Advances in Civil Engineering*, vol. 2020, 15 pages, 2020.
- [21] X. Q. Yuan, Z. Duan, and F. S. Zhao, "The Formation Mechanism of River Erosion-Induced Loess Landslide," *IOP Conference Series: Earth and Environmental Science*, vol. 186, 2018.

- [22] Z. Wang, B. Liu, Y. Han, J. Wang, B. Yao, and P. Zhang, “Stability of inner dump slope and analytical solution based on circular failure: illustrated with a case study,” *Computers and Geotechnics*, vol. 117, article 103241, 2020.
- [23] Y. He, H. Zhang, B. Liu, and Y. Wu, “Research on FLAC 3D numerical simulation of working mechanism of compaction pile composite foundation,” *Applied Mechanics and Materials*, vol. 204-208, pp. 220–223, 2012.
- [24] W.-c. Wang, S.-r. Sun, J.-h. Wei, Y.-x. Yu, W. He, and J.-l. Song, “Numerical experimental study on optimum design of anchorage system for Xiashu loess slope,” *Journal of Central South University*, vol. 28, no. 9, pp. 2843–2856, 2021.
- [25] P. Zhang, D. Zhang, Y. Yang et al., “A case study on Integrated modeling of spatial information of a complex geological body,” *Lithosphere*, vol. 2022, no. Special 10, article 2918401, 2022.
- [26] D. Chen, H. Chen, W. Zhang, J. Lou, and B. Shan, “An analytical solution of equivalent elastic modulus considering confining stress and its variables sensitivity analysis for fractured rock masses,” *Journal of Rock Mechanics and Geotechnical Engineering*, 2021.
- [27] D. Peng, Q. Xu, F. Liu et al., “Distribution and failure modes of the landslides in Heitai terrace, China,” *Engineering Geology*, vol. 236, pp. 97–110, 2018.
- [28] H. Deng, L. Z. Wu, R. Q. Huang, X. G. Guo, and Q. He, “Formation of the Siwanli ancient landslide in the Dadu River, China,” *Landslides*, vol. 14, no. 1, pp. 385–394, 2017.
- [29] Q. Meng, W. Li, F. Raspini et al., “Time-series analysis of the evolution of large-scale loess landslides using InSAR and UAV photogrammetry techniques: a case study in Hongheyuan, Gansu Province, Northwest China,” *Landslides*, vol. 18, no. 1, pp. 251–265, 2021.
- [30] Z.-j. Meng, P.-h. Ma, and J.-b. Peng, “Characteristics of loess landslides triggered by different factors in the Chinese loess plateau,” *Journal of Mountain Science*, vol. 18, no. 12, pp. 3218–3229, 2021.